Electronic Supplementary Material (ESI) for Nanoscale.

Supporting Information:

Layer by layer grown scalable redox-active ruthenium-based molecular multilayer thin films for electrochemical applications and beyond

Veerabhadrarao Kaliginedi, [†]* Hiroaki Ozawa,[‡] Akiyoshi Kuzume,[†]* Sivarajakumar Maharajan, [§] Ilya V. Pobelov, [†] Nam Hee Kwon,[§] Miklos Mohos, [†] Peter Broekmann, [†] Katharina M. Fromm, [§]* Masa-aki Haga, [‡]* Thomas Wandlowski[†]

[†] Department of Chemistry and Biochemistry, University of Bern, Freiestrasse 3, CH-3012 Bern, Switzerland.

[‡] Department of Applied Chemistry, Faculty of Science and Engineering, Chuo University, Bunkyo-ku, Tokyo 112-8551, Japan.

[§] Department of Chemistry, University of Fribourg, Chemin du Musée 9, CH-1700 Fribourg, Switzerland.

Table of contents:

1. Synthesis procedure.

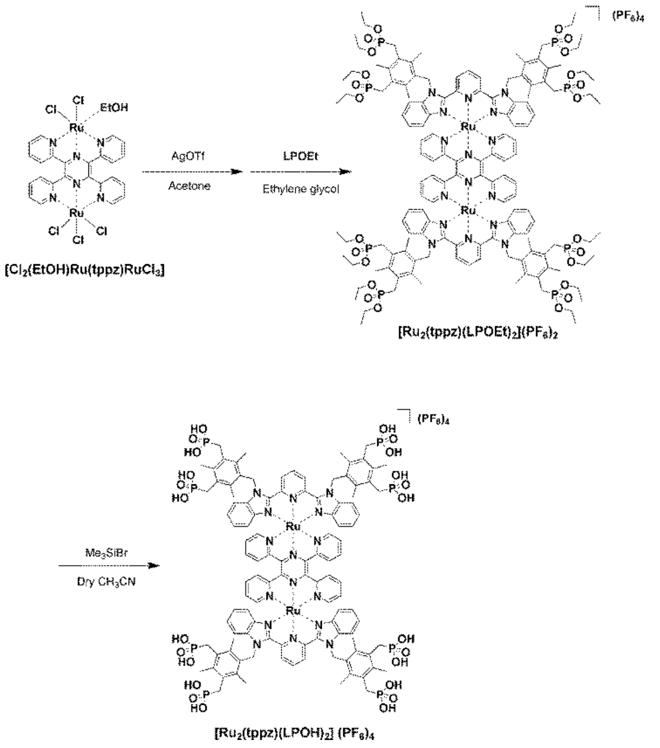

Scheme 1: Synthetic route to synthesize [Ru$_2$(tppz)(LPOH)$_2$] (PF$_6$)$_4$.

[Ru$_2$(tppz)(LPOEt)$_2$](PF$_6$)$_2$: To 50 mL of dry acetone were added [Cl$_2$(EtOH)Ru(tppz)RuCl$_3$] (100 mg, 0.12 mmol) and AgOTf (155 mg, 0.6 mmol). The mixture was refluxed for 2 h before it was cooled to room temperature. The precipitate was removed by Celite filtration, and the filtrate was concentrated to dryness. To the blue-violet residue were added LPOEt (400 mg, 0.34 mmol) and ethylene glycol (10 mL). The mixture was then refluxed for 4 h. After it was cooled to room temperature, the resulting solution was diluted by addition of saturated KPF$_6$ aq (10 mL). The resulting precipitate was collected by filtration. The crude product was purified by column chromatography on Sephadex LH 20 (eluent: CH$_3$CN/MeOH, 1/1 v/v) to give the blue solid (320 mg, 71%). ^{1}H NMR (500 MHz, CD$_3$CN): 9.07 (d, 4H, J = 8.0 Hz), 8.79 (d, 4H, J = 8.0 Hz), 8.69 (t, 2H, J = 8.3), 8.05 (d, 4H, J = 4.6 Hz), 7.83 (t, 4H, J = 7.7 Hz), 7.52 (t, 4H, 6.6 Hz), 6.86 (t, 4H, J = 8.6 Hz), 6.64 (d, 4H, J = 8.6 Hz), 6.48 (m, 8H), 6.42 (m, 8H), 3.92 (m, 32H), 3.35 (d, 16 H, J =10.0 Hz), 2.47 (s, 12H), 2.28 (s, 24H), 1.17 (m, 48 H). ESI-TOF MS: *m/z* 735.7. $[M\text{-}4PF_6]^{4+}$ Calcd for $C_{142}H_{178}N_{16}O_{24}P_8Ru_2$: 735.7. Anal. Calcd for $C_{142}H_{178}F_{24}N_{16}O_{24}P_{12}Ru_2 \cdot 6H_2O$: C, 46.97; H, 5.27; N, 12.56. Found: C, 46.66; H, 4.98; N, 6.27.

$[Ru_2(tppz)(LPOH)_2]$ $(PF_6)_4$: To complex $[Ru_2(tppz)(LPOEt)_2](PF_6)_2$ (50 mg, 15 μmol) in 15 mL of anhydrous CH_3CN, Me_3SiBr (600 uL) was added and the mixture was stirred under nitrogen at 60 °C for 14 h. To the resulting solution, excess MeOH was added to decompose the protected group, and the solvent was evaporated. After washing the residue with acetonitrile, the residue was dissolved in small amounts of methanol, followed by the addition of HCl and the excess amount of aqueous solution of KPF_6 to afford a blue precipitate of $[Ru_2(tppz)(LPOH)_2]$ $(PF_6)_4$, which was collected and dried in vacuo (30 mg, 61%). Anal. Calcd for $C_{110}H_{114}F_{24}N_{16}O_{24}P_{12}Ru_2 \cdot 5H_2O$: C, 41.76; H, 3.95; N, 7.08 %. Found: C, 41.57; H, 4.18; N, 6.87.

2. Cyclic voltammetry in aqueous electrolyte.

Electrochemical measurements were conducted at room temperature using a lab-built potentiostat. A custom designed, single compartment glass cell was used for voltammetric measurements. Two platinum wires were used as the counter and quasi-reference electrodes, where 0.1 M $HClO_4$ was used as an electrolyte. Platinum quasi-reference electrode was calibrated using a true reference electrode Ag/AgCl with a potential difference of 610 ± 10 mV measured under the same experimental conditions. All the electrochemical measurements were performed under argon atmosphere.

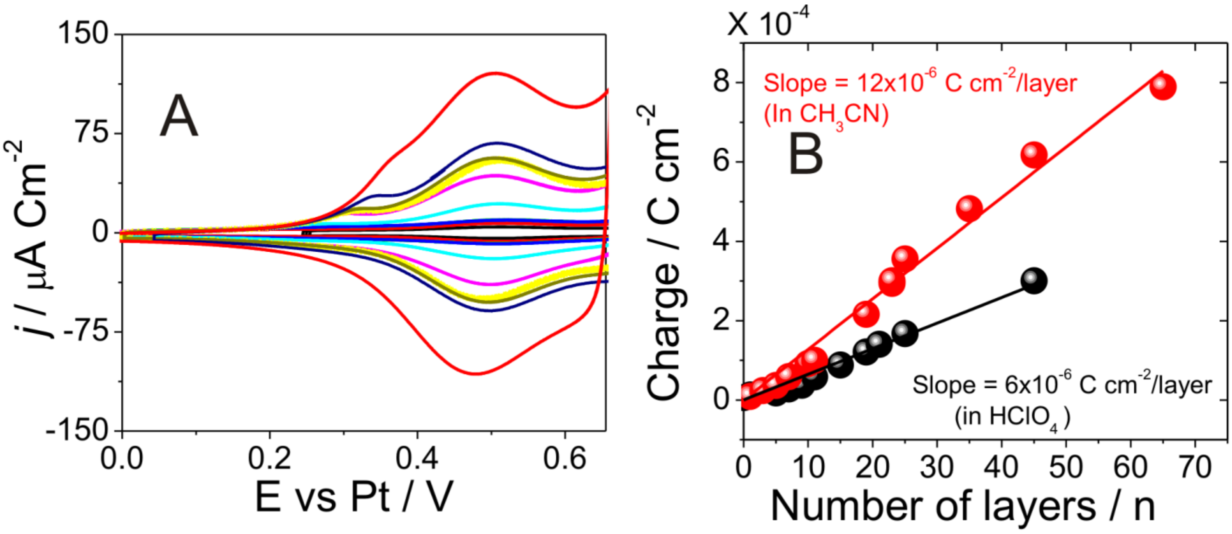

Figure.S1: (A) Cyclic voltammograms (CVs) of the Ru complex multilayers (ITO|(Ru-N)n) with different number (n = 1 - 45) of layers in 0.1 M $HClO_4$ at a scan rate of 100 mV s^{-1} on the ITO electrode. (B) Plot of total integrated charge from cyclic voltammetry experiment as a function of number of layers measured in aqueous electrolyte and non-aqueous CH_3CN electrolyte at a scan rate of 100 mV s^{-1}.

The cyclic voltammograms measured in aqueous electrolyte showed only one redox peak corresponding to the one electron redox process (i.e., a Ru(II)-Ru(II) /Ru(III)-Ru(II)) couple and second redox process for a Ru(III)-Ru(II)/Ru(III)-Ru(III) couple is not accessible in aqueous electrolyte, which was observed in non-aqueous CH_3CN (See Fig. S1A and Fig. 2A in the main text). It is also evident from the total integrated charge extracted from the cyclic voltammograms measured in aqueous and non-aqueous electrolytes (Fig.S1B).

The total integrated charge obtained from cyclic voltammetry experiment increases as a linear function of layer's number with a slope of 12×10^{-6} C cm^{-2} / layer in the non-aqueous and 6×10^{-6} C cm^{-2} / layer in the aqueous electrolyte, the latter is equivalent to the one-electron charge of one full monolayer (full monolayer coverage is equivalent to $\approx 5.8 \times 10^{-11}$ mol/cm^2) (see Fig. S1B). The total integrated charge did not show saturation with the increase in the layer thickness. The values of slopes indicate the addition of one full monolayer at each step of the layer by layer assembly process. This result further confirms the successful formation of uniform multilayer films on ITO substrate.

3. Electrochemical Quartz Crystal Microbalance (EQCM) experiments.

The EQCM technique is a powerful tool for detecting very small mass changes at the electrode surface accompanying electrochemical processes.[1,2] An AT cut quartz crystal resonator coated with very thin ITO electrode pads were used in our measurements. Layer-by-layer self-assembly procedure as described in the main text was applied for the fabrication of ruthenium complex multilayers on ITO-coated quartz crystal resonator. Fig. S2A displays a typical cyclic voltammogram and a frequency response of Ru-N films on ITO-coated quartz crystal resonator electrode (9 layer of Ru-N) in 0.1 M $HClO_4$ in CH_3CN recorded with potential sweep rate 50 mV s^{-1}. When the potential was scanned in the positive direction, a decrease in frequency (ΔF) was observed, followed by the electrochemical oxidation from the Ru(II)-Ru(II) state to the Ru(III)-Ru(III). The frequency change during the potential sweep indicates that a mass change took place on the electrode surface. The mass change of the electrode with respect to the electrode potential can be estimated by Sauerbrey equation.

$$\Delta F = -\frac{2\ F^2 \Delta m}{\sqrt{\mu\rho}\, n\ \ A} = -2.2640 \times 10^{-6} F^2 \frac{\Delta m}{A}$$

where “m/A” is the mass per unit area (A = 0.196 cm^2), n is the harmonic number of the oscillation (n = 1), $\mu = 2.947 \times 10^{11}$ g cm^{-1} s^{-2} is the shear modulus of quartz and $\rho = 2.648$ g cm^{-3} is the density of quartz. Fig.S2B shows the plot of the frequency and the mass change during potential sweep vs the number of Ru-N layers, which shows a linear increase with a slope of 3.74 ng cm^{-2} per layer. We attribute the frequency decrease and the mass increase in

EQCM measurements to the anion penetration into the ruthenium multilayer film in order to neutralize the charge imbalance created upon the oxidation of Ru(II)-Ru(II) to Ru(III)-Ru(II) and further oxidation to the Ru(III)-Ru(III) state. The frequency/mass change is totally reversible (see Fig. S2A) with respect to the electrode potential, which indicates the reversible incorporation/removal of anion into/out of the multilayers. Similar results were also reported by Shinomiya *et al.*[1]

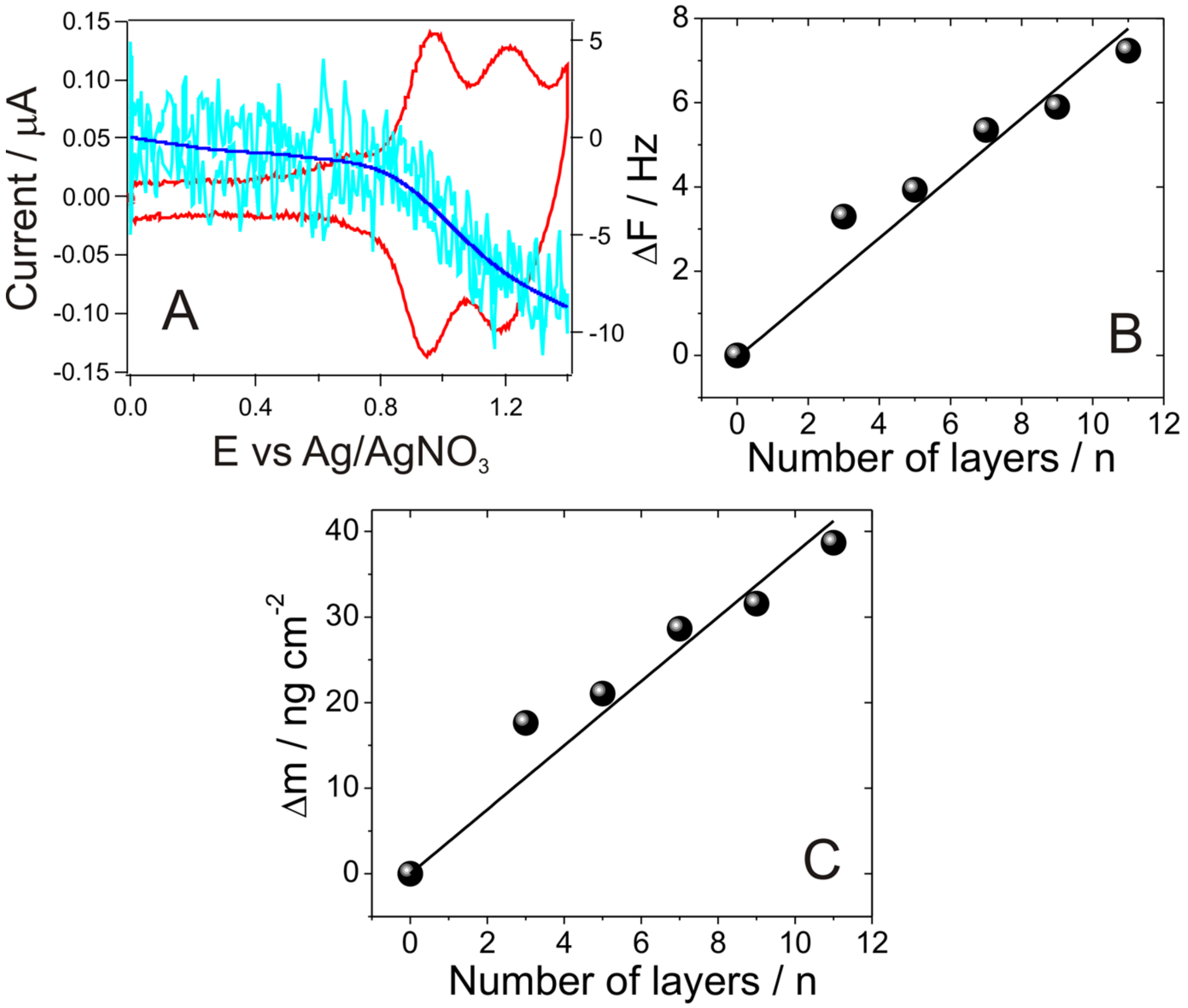

Figure.S2: (A) Typical cyclic voltammograms and frequency response of Ru-N films on ITO electrode (9 layer of Ru-N) in 0.1 M $HClO_4$ in CH_3CN, scan rate 50mV s^{-1}. (B) Frequency and (C) mass change vs the number of Ru-N layers.

4: *Ex situ* AFM imaging and scratching experiments.

AFM imaging was carried out in an ambient environment at room temperature employing FlexAFM scan head (10 µm scan range) with C3000 controller (Nanosurf) in dynamic mode using PPP-NCHAuD cantilevers (Nanosensors). The surface of bare ITO after RCA treatment (Fig. S3A) demonstrates relatively flat (root mean square area roughness $S_{rms} < 0.5$ nm) grains with the size of up to few hundreds of nm, which are separated by trenches and holes. The trenches are typically 2-3 nm deep, the hole depths vary between 5 and 8 nm. S_{rms} obtained for the area in Fig.S3A is 0.99 nm. Fig. S3B displays the surface of the ITO sample with 65 layers of Ru complex assembled. Interestingly, the modified surface displays no signs of trenches and holes present on ITO support, which might indicated that the defects in ITO surface were covered by assembled Ru complex molecules. $S_{rms} = 2.1$ nm obtained for the area in Fig. S3B is only slightly higher than that for the area in Fig. S3A.

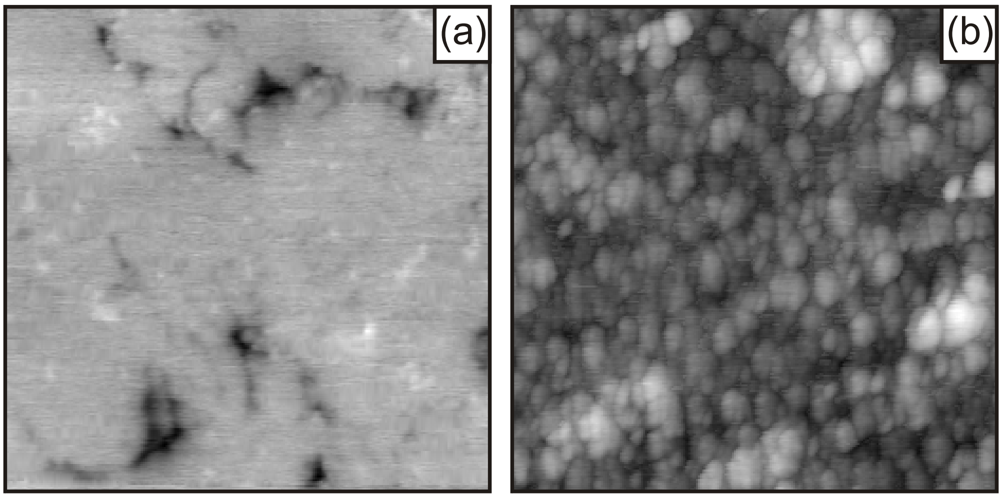

Figure.S3: AFM images of (A) bare ITO and (B) ruthenium complex multilayer (n = 65). The lateral sizes are 1 µm × 1 µm, the vertical scales (from black to white) are 12 nm (a) and 18 nm (b).

To determine the thickness of the layers, a 1 µm ×1 µm area was scanned in the contact mode with a high applied force. During this scanning the layer was completely "scratched" down from the surface by the tip. Afterwards a bigger area was scanned in dynamic mode to determine the depth of the scratched area and therefore the layer thickness. Fig.S4 shows the correlation between the layer thickness and the numbers of the building blocks in the single layers.

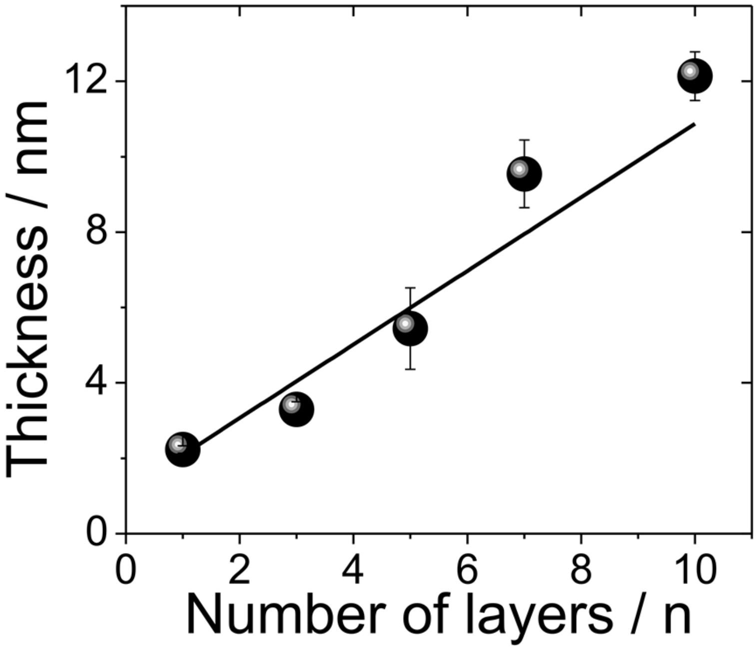

Figure.S4: Layer thickness extracted form AFM scratching profiles vs number of layers on ITO substrate.

Due to the non-uninform topography of the ITO substrate (presence of holes and trenches), AFM scratching experiment results give large error bars. To avoid surface roughness problems, we performed the AFM scratching experiment on ultra-flat sapphire (Al_2O_3) substrate, which surface binds to phosphonate linker group in the same way as ITO. AFM scratching experiments were carried out on multilayers prepared on sapphire substrate under similar conditions as used for fabrication of multilayers on ITO (Fig. S5).

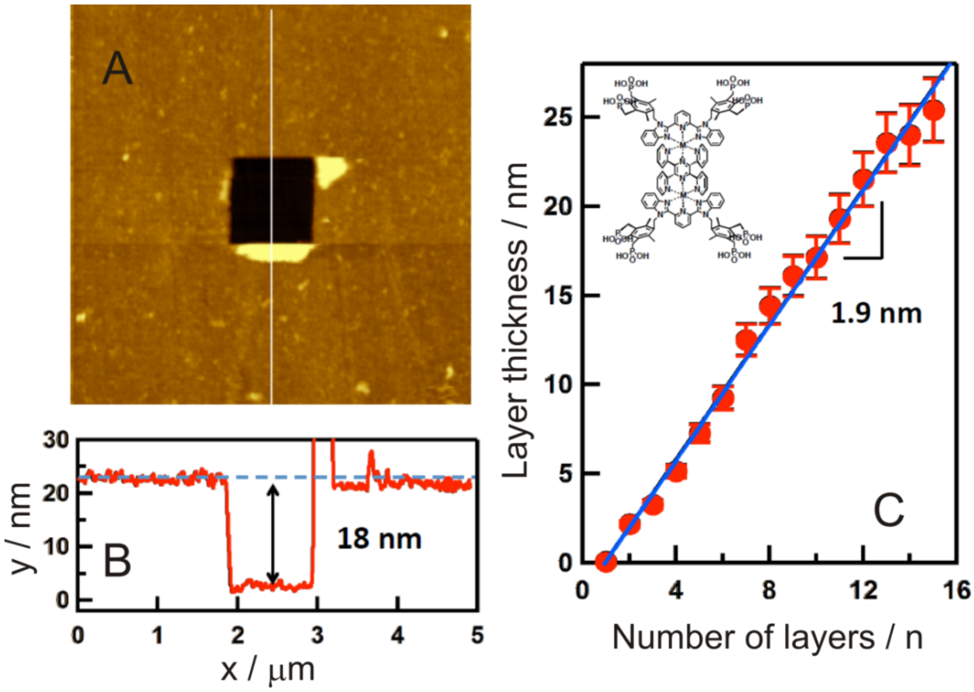

Figure.S5: AFM scratching experiment of ruthenium complex multilayers on sapphire substrate (sapphire|(Ru-N)$_n$) fabricated by layer-by-layer (LBL) assembly technique. (A) AFM image of a ruthenium complex multilayer film (*n* = 10) on a sapphire substrate with a scratch made by AFM cantilever operated in contact mode. (B) Cross section profile of the AFM image along the white line shown in the panel A. (C) Layer thickness extracted form AFM scratching profiles vs number of layers.

Fig.S5A and S5B displays an AFM image of a ruthenium complex multilayer film (*n* = 10) on a sapphire substrate with a scratch made by AFM cantilever operated in contact mode (Agilent Technologies 5500 AFM microscope and NanoWorld NCHR-20 silicon cantilever with a force constant of 42 N m^{-1} were employed) and cross section profile of the AFM image along the white line. For the scratching, the cantilever loading force was set to 3.4 µN. After each scan at the preset loading force for the scratching, we zoomed out to scan a larger area at an imaging force of 97 nN. Fig.S5C displays plot of layer thickness extracted form AFM scratching profiles vs number of layers with a slope of 1.9 nm/layer, which is very close to the molecular length (2.3 nm) value calculated from the molecular modelling. These results strongly indicate that uniform films were formed on the ITO or sapphire substrate and strongly support the aforementioned cyclic voltammetry results (Fig.S1B). Small discrepancy in layer thickness is observed due to the error bars (up to 25 %) associated with AFM scratching experiment.[1,3,4] These errors may arise from noise and image distorted effects due to the presence of nonlinearities in the piezo of the scanner.[3]

In addition to the layer thickness analysis, these AFM experiments demonstrate the applicability of the layer by layer assembly procedure utilizing phosphonic acid anchoring groups on different conductive (ITO) and non-conductive (sapphire) oxide substrates. As we employed ITO on glass, there is a possibility to form during the assembly process ruthenium complex layers also on glass side. Interestingly, we also found evidences (*In situ* Raman experiment and in-situ UV-Vis measurements, see the following sections for details) for formation of ruthenium complex multilayer on glass.

5. In-situ potential-dependent UV-Vis spectroscopy and resonance Raman spectroscopy experiments.

In-situ UV-Vis spectroelectrochemistry results shown in Figure S6 and data reported by Nagashima *et al.*,[5] showed clear spectral changes due to the well-separated one-electron two-redox processes occurred in the multilayer (Ru(II)−Ru(II)/Ru(II)−Ru(III) and Ru(II)−Ru(III) / Ru(III)−Ru(III) couples). Oxidative spectroelectrochemistry of ruthenium complex revealed that the first oxidation at +0.30 V vs Pt led to the diminishing intensity of the MLCT band at 576 nm. A clear blue shift of MLCT band after the first oxidation was observed by Nagashima *et al.*, in bulk spectroelectrochemistry experiment, i.e. with Ru complex dissolved in non-aqueous solution. The blue shift was not clear in our experiment, however we observed a clear broadening of the MLCT band at 576 nm (see Fig. S6). Further oxidation at +0.63 V resulted in further decrease in MLCT band at 576 nm and $\pi\pi^*$ band at 357 nm. In contrary, Nagashima *et al.*,[5] observed the complete loss of this MLCT band at 576 nm and decrease of ππ* band at 357 nm after the second oxidation. We attribute the difference between spectroelectrochemistry of dissolved Ru complex (Nagashima *et al*[5]) and of the assembled layer to the absorbance contribution of the Ru complex assembled on glass side of the electrode. Insert of Fig.S6 shows the cyclic voltammogram recorded in the spectroelectrochemistry cell and the MLCT band at 0.68 V before (pink) and after (orange) the subtraction of absorbance contribution from the ruthenium complex multilayer assembled on the glass side (by assuming 50 % contribution from glass side). These results clearly demonstrate that the ruthenium complex layer assembled on the conducting ITO side of the glass plate shows a loss of MLCT band after the second oxidation, i. e, at 0.63 V. On the other hand, ruthenium layers assembled on the glass side do not feel electric field, so they did not show any spectral change with the change of the electrode potential.

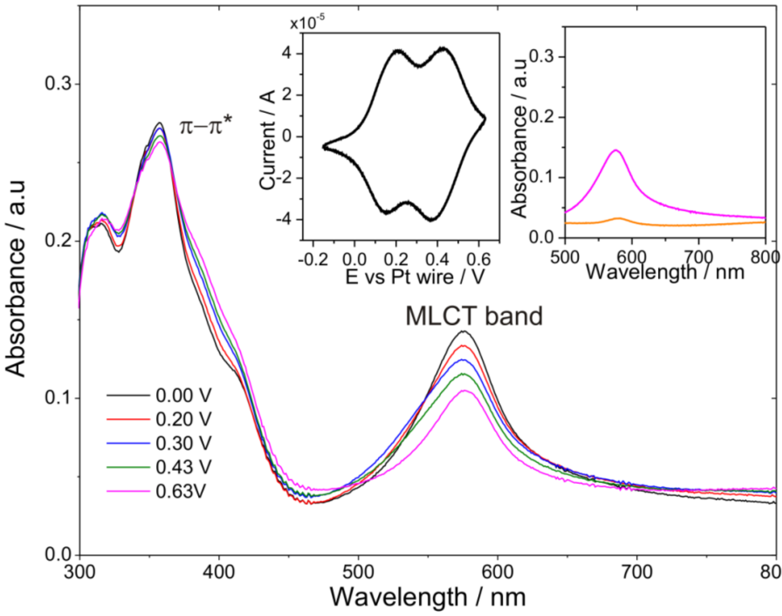

Figure.S6: Potential-dependent UV-Vis spectra of the Ru complex multilayer (*n* = 35) on ITO electrode in 0.1 M $HClO_4$ in CH_3CN solution. Inserts shows the cyclic voltammogram recorded in the spectroelectrochemistry cell and the MLCT band at 0.63 V vs Pt reference electrode before (pink) and after (orange) the subtraction of absorbance contribution from the ruthenium complex multilayer assembled on the glass side.

Figure S7 shows potential-dependent resonance Raman spectra of Ru complex multilayer (*n* = 65) in 0.1 M $HClO_4$ in CH_3CN with 532.8 nm excitation. Due to the MLCT band of Ru complex multilayer observed at 576 nm in UV-Vis spectra (Fig. S6 and Fig. 2 of the main text of the paper), the Raman signals are specifically enhanced by the resonance effect, which is caused by using the excitation wavelength (532 nm) near the electronic vibration of the sample. The band assignments of Ru complex multilayer are summarised in Table.S1.[6]

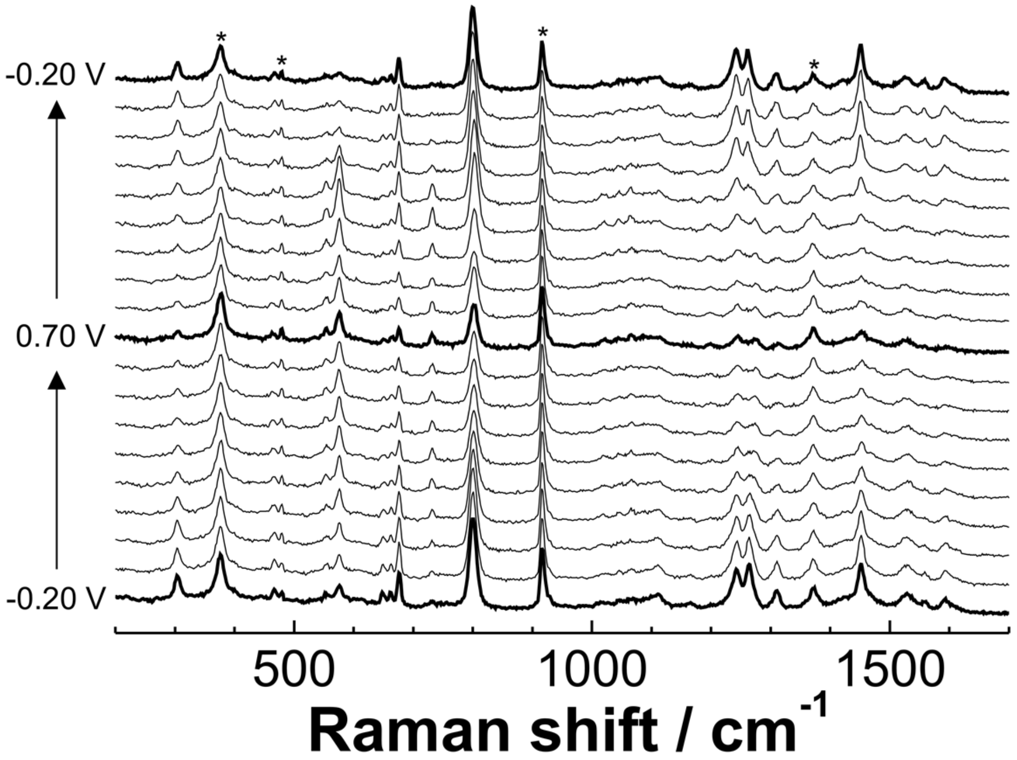

Figure.S7: Potential-dependent resonance Raman spectra of the Ru complex multilayer (*n* = 65) on ITO electrode in CH_3CN with 0.1 M $HClO_4$ as electrolyte. The direction of the potential scan is indicated by the arrows. Peak assignments are summarised in Table.S1.

Reference Raman spectra of ITO electrode under electrochemical control were acquired in the absence of Ru complex multilayer in 0.1 M $HClO_4$ in CH_3CN electrolyte (Fig. S8). Two broad features observed around 600 and 1100 cm^{-1} as well as a small peak at 480 cm^{-1} are due to the ITO substrate. These features are overlapping with three peaks at 377, 916 and 1371 cm^{-1} that are assigned to C-C-N bending, C-C stretching and CH_3 in-phase bending modes from solvent molecules (Fig. S8). The positions of these background features do not shift with potential.

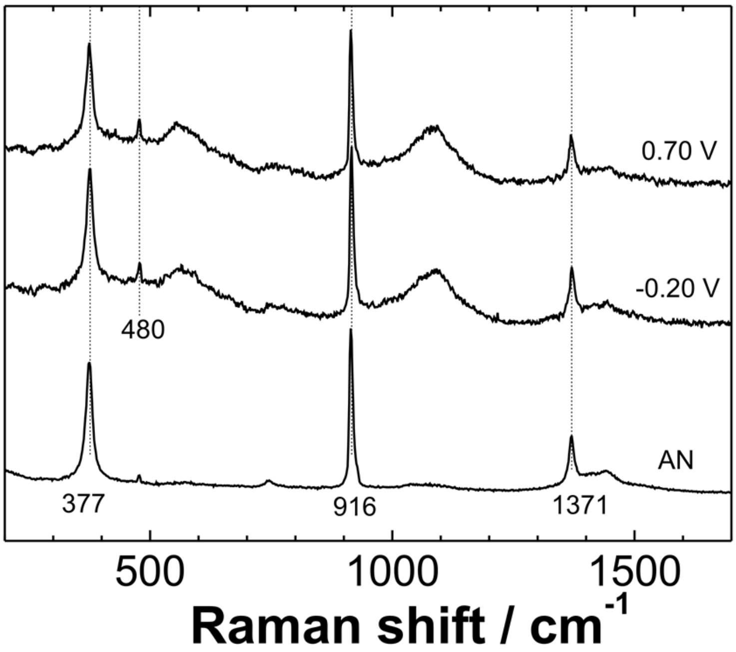

Figure.S8: Raman spectra of ITO electrode in the absence of Ru complex multilayer acquired at 0.70 (top) and -0.20 V (middle) (vs Pt wire) in 0.1 M $HClO_4$ in CH_3CN solution and the normal Raman spectrum of CH_3CN (bottom) for the reference.

A band at 304 cm^{-1} is assigned to a Ru-N stretching mode (ν(Ru-N)).[6b] The spectral features of this band should change with the redox state of Ru metal centres. However, the band position of ν(Ru-N) does not change with potential. On the other hand, the intensity of ν (Ru-N) decreases during the first oxidation process ($0.00 \leq E \leq 0.30$ V), and further gradual decrease was observed during the second oxidation process ($0.30 \leq E \leq 0.70$ V). This behaviour is reversible during multiple potential cycles between -0.20 and 0.70 V. Most of Raman bands observed in Fig.S7 show spectral behaviour similar to that of ν(Ru-N) (Fig. S9A) with some exception. The decrease in Raman intensity of the peaks with the increase of the electrode potential clearly correlates with the decrease and loss of MLCT band at 576 nm in spectroelectrochemistry experiment during the oxidation from Ru(II)-Ru(II) to Ru(III)-Ru(II) and further to Ru(III)-Ru(III) (Fig. S6). In particular, the intensities of 576 and 732 cm^{-1} bands increase during the first oxidation process, reaching maximum at 0.30 V, then decrease during the second oxidation process. This clearly correlates with observations made by Nagashima *et al.*: blue shift of MLCT band after the first oxidation may be enhancing the Raman vibrations at 576 and 732 cm^{-1}. Further oxidation leads to the loss of MLCT band, which lead to the decrease in Raman intensity of 576 and 732 cm^{-1}. In addition, for all bands there was no position shift with potential (Stark effect). Nonetheless, *in situ* potential-dependent Raman spectra show clear reversible structural reorganization during the potential cycling.

It is interesting to point out that the strong band at 990 cm^{-1} due to the vibration mode of aromatic carbon radial, which was one of the strongest Raman bands in both TPPZ and BPP linker molecules,[6a,f] was not observed in the Raman spectra of Ru complex multilayer (Fig. S7). This is due to the formation of coordination bonds between nitrogen atoms and Ru metal centers, which limits the structural symmetry of the aromatic vibration mode. Together with the emergence of ν(Ru-N) band, the lack of band at 990 cm^{-1} in the whole potential range is a clear evidence for the high stability of Ru complex under the electrochemical condition in this potential range.

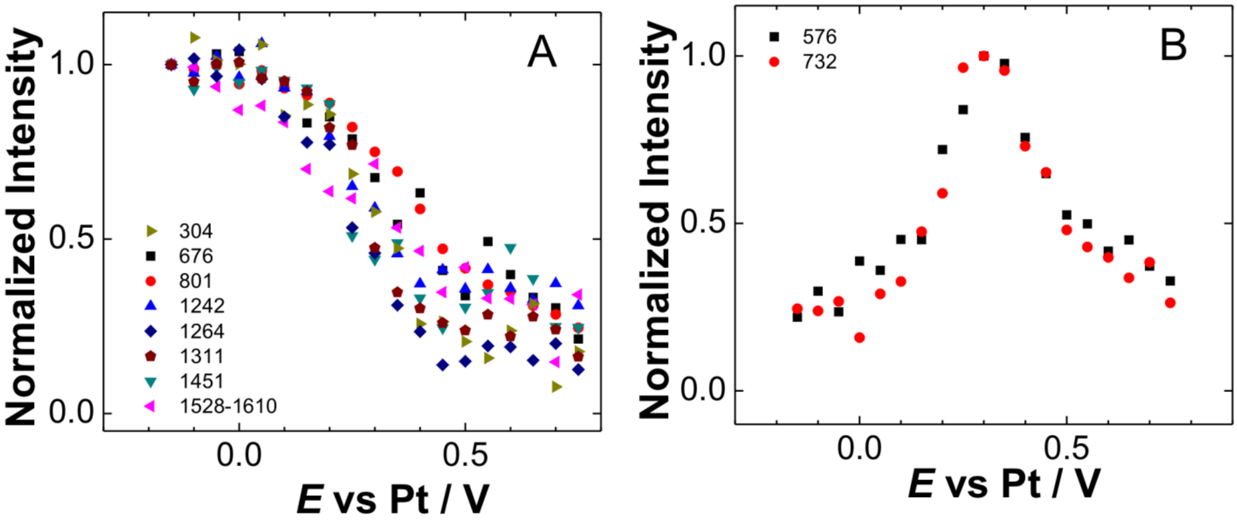

Figure.S9: Potential dependent normalized band intensity plots obtained from the anodic scan in the Fig. S7.

Two-dimensional Raman correlation spectroscopy was used to analyse the correlation between the potential sweep and a change in band intensities for Raman bands observed in Fig. S7. The peak positions on the 2-D correlation spectral plane are used to study intra- and inter-molecular interaction in correlation with a potential sweep.[7] 2-D Raman correlation spectrum acquired from potential-dependent Raman spectra shows correlation between main bands correlate each other, while no correlation between some small peaks, such as 467, 649, 663, 1045, 1111 and 1198 cm^{-1} were depicted in Fig.S10. The intensity of these bands does not change with potential, indicating no participation of these bands in the redox processes of Ru-N complex multilayer.

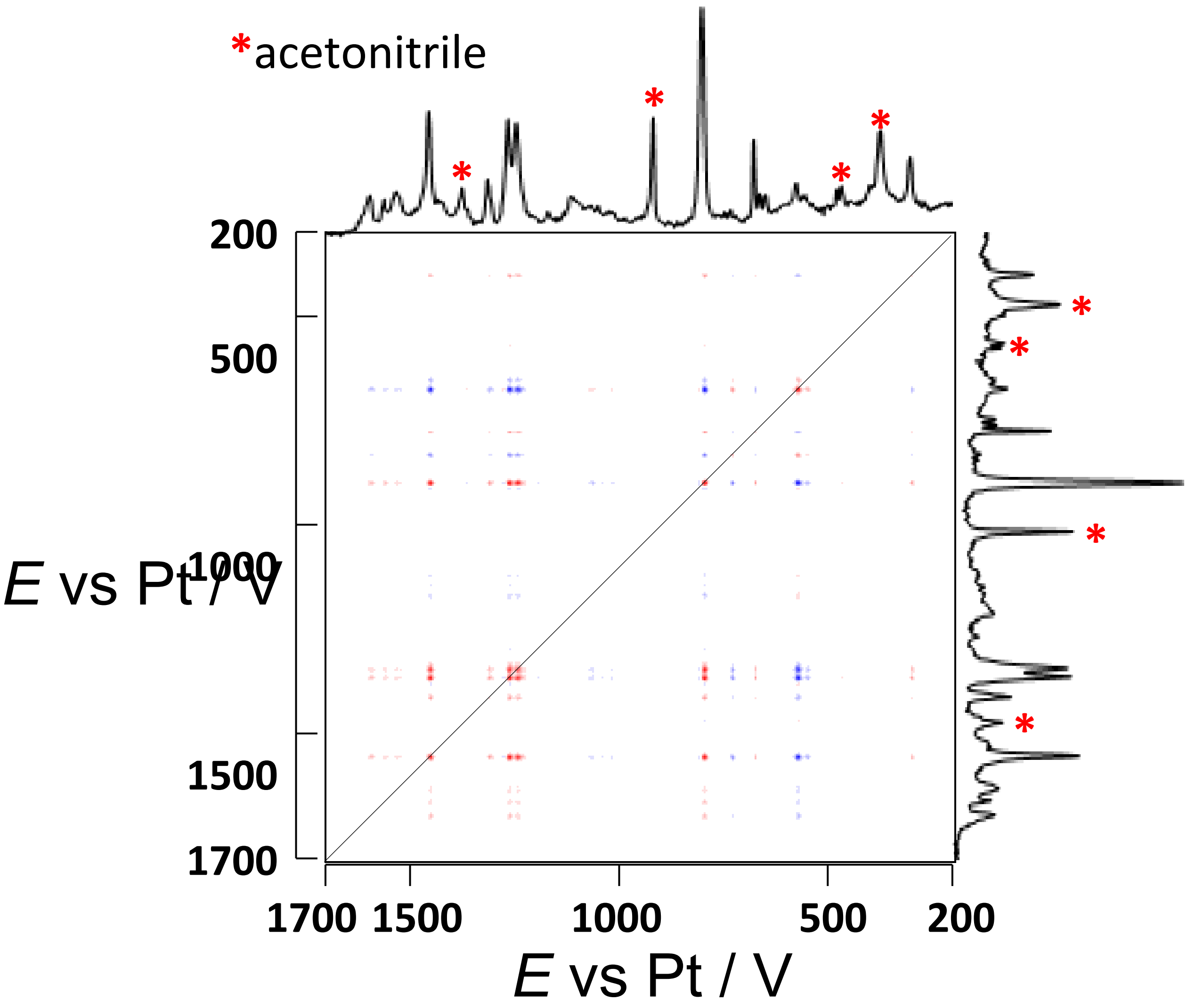

Figure.S10: Synchronous two-dimensional Raman correlation spectrum of Ru complex multilayer (n = 65) acquired from data in potential dependent Raman spectra (Fig. S7) using 2Dshige software (version 1.3).[8]

Table.S1: Observed Raman frequencies for Ru complex multilayer (*n* = 65) in 0.1 M $HClO_4$ acetonitrile solution and their assignment.

Frequency (cm^{-1})	*descript*	*Assignment*
304	ν(*Ru-N*)	Ru-N stretching
*377	δ(*CCN*)	C-C-N bending (AN)
467	δ (*PF*$_6$*)*	symmetric bending (PF_6)
*480	-	ITO
554	δ(*NCN)o.pl.*	N-C-N out-of-plane deformation (Imidazole part)
576	δ(*ring) o.pl.*	Ring out-of-plane deformation (BBP)
649	-	-
663	-	-
676	δ(*ring) i.pl.*	Ring in-plane deformation
732	δ (*ring)*$_{1/4}$ *i.pl.*	Quadrant ring in-plane bending (Pyrazine part in TPPZ)
801	δ (*CH) o.pl.*	Aromatic C-H out-of-plane deformation
*916	ν(*CC*)	C-C stretching (AN)
1020	δ (*CH) i.pl.*	C-H in-plane bending
1045	-	-
1065	δ (*ring), or* δ(*CH) i.pl.*	Ring bending (Imidazole part in BPP) or C-H in-plane bending (Pyridine part in TPPZ)
1111	-	-
1198	-	-
1242	δ (*CH) i.pl. + ring breath*	C-H in-plane bending + ring breathing (BPP)
1264	δ (*CH) i.pl.* + ν(*ring)*	C-H in-plane bending + ring stretching (BPP)
1311	δ (*CH) i.pl.*	C-H in-plane bending (Pyridine species in TPPZ)
*1371	δ(*CH*$_3$*)*	CH_3 in-phase bending (AN)
1451	ν(*ring)*$_{1/2}$	Semicircle ring stretching (phenyl species in BPP)
1528	ν(*ring)*$_{1/4}$	Quadrant ring stretching (Pyrazine species in TPPZ)
1558	ν(*ring)*$_{1/4}$	Quadrant ring stretching (Pyridine species)
1592	ν(*ring)*$_{1/4}$	Quadrant ring stretching (Pyridine species)

6. Thermal stability test

Figure S11A displays the cyclic voltammograms (CVs) of freshly prepared ITO|(Ru-N)$_7$ sample (black) and ITO|(Ru-N)$_7$ sample (red) which was stored under ambient conditions for 90 days. No redox potential change or charge change was observed between the freshly prepared sample and the 90 days old sample. These results clearly demonstrated the stability of ruthenium complex multilayer films under ambient conditions. We also tested the thermal stability of the ITO|(Ru-N)$_7$ sample by heating it on a hot plate at 150^{o}C (in air) and measured the cyclic voltammogram of the heated sample. Figure S11B shows the cyclic voltammograms (CVs) of freshly prepared ITO|(Ru-N)$_7$ sample (black) and same sample heated on a hot plate at 150^{o}C for 30 minutes. There is no significant change in redox potentials were observed, however a small change in the charge was observed may be due the small loss in the material or surface oxidation during the heating process.

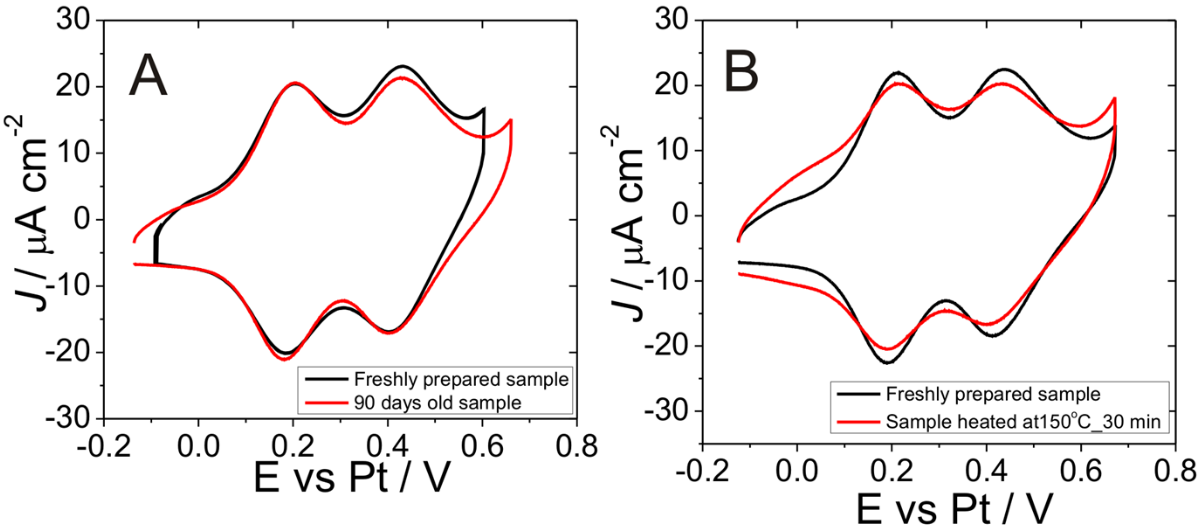

Figure.S11: Thermal stability test of ITO|(Ru-N)$_7$. (A) Cyclic voltammograms (CVs) of freshly prepared ITO|(Ru-N)$_7$ sample (black) and ITO|(Ru-N)$_7$ sample (red) which was stored under ambient conditions for 90 days. (B) Cyclic voltammograms (CVs) of freshly prepared ITO|(Ru-N)$_7$ sample (black) and same sample heated on a hot plate at 150^{o}C for 30 minutes.

7. Ex-situ XPS measurements

Ex-situ X-ray photoelectron spectra of ITO|(Ru-N)$_n$ multilayer samples were measured by using a Shimadzu/Kratos Axis HSi spectrometer with monochromated Al Kα radiation as an excitation source. Figure S12 displays the ex-situ XPS spectra for ITO|(Ru-N)n (n = 0 ~3). The signal intensities for the O1s, Sn 3d, In 3d, In 4s peaks from the substrate were gradually decreased with increasing the ITO|(Ru-N)n layer thickness. On the other hand, the signal intensities for N1s, C1s, Ru 3d, P 2p peaks were increased with increasing the thickness of the ITO|(Ru-N)$_n$ layers. Presence of Ru 3d signals confirmed the "+2" oxidation state of the ruthenium centre in the multilayer film. No Zr 3d signal was observed for bare ITO, n=1 sample and Zr 3d signals were observed from bilayers (n= 2), confirming the Zr ion incorporation into the layers. The intensity ratio of Zr/Ru 11.8 was observed. Even though the Ru-N complex was isolated as $[PF_6]^-$ salts, the signal for F was hardly observed in the XPS spectra. However, we found a clear Raman peak for $[PF_6]^-$ at around 467 cm^{-1} wavenumber corresponding to the symmetric bending of $[PF_6]^-$ and other peak at 568 cm^{-1} corresponding to stretching is overlapping with the background signal (Fig. S7 and Table. S1). This confirms the presence of $[PF_6]^-$ in the layers.

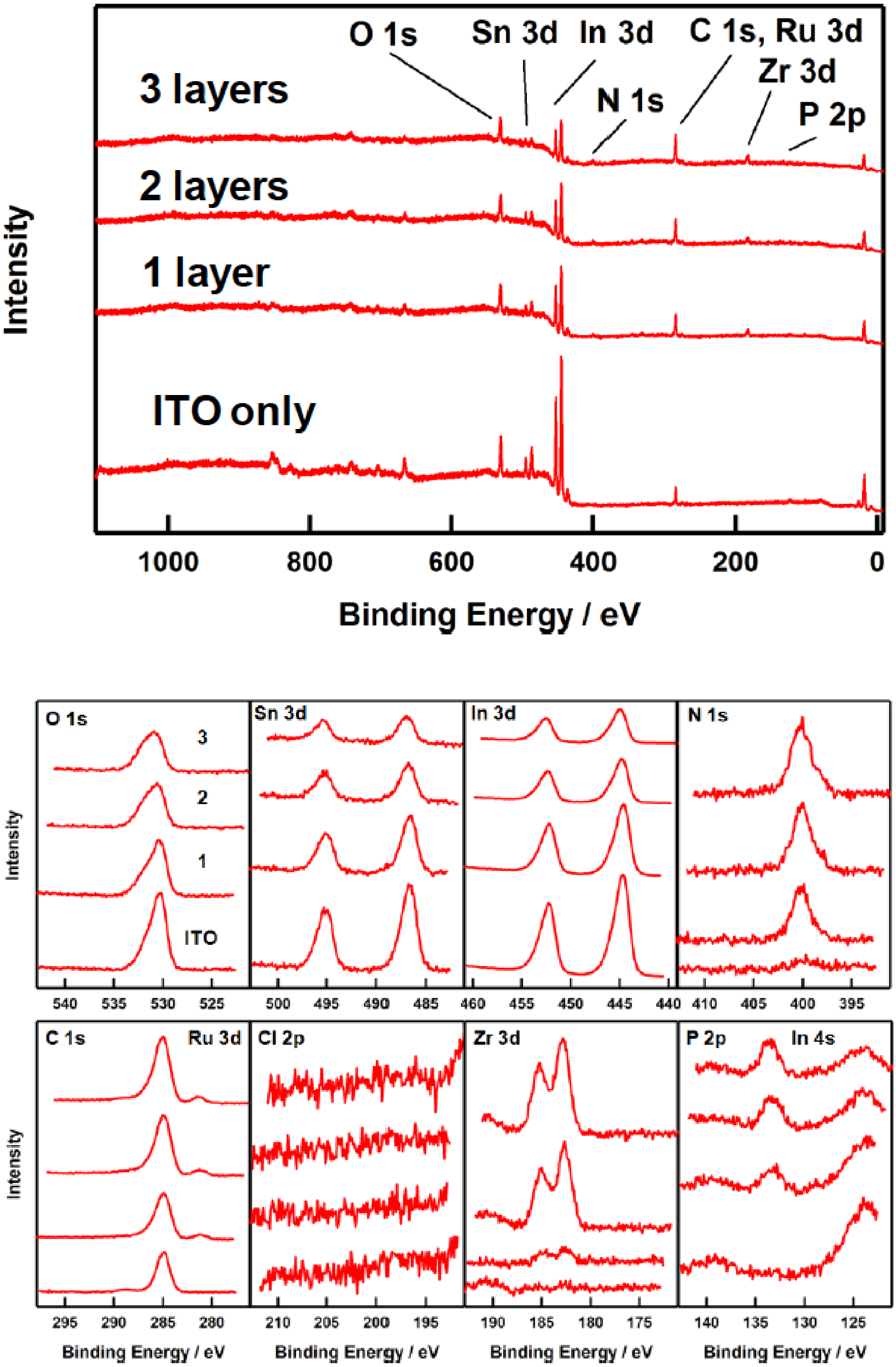

Figure.S12: *Ex-situ* XPS spectra of ITO|(Ru-N$)_n$ (n= 0~3): wide scan spectra (top) and narrow O 1s, Sn 3d, In 3d, N 1s, C 1s, Cl 2p, Zr 3d, and P 2p region(bottom).

8. Data analysis for electrochemical energy storage application

Cyclic Voltammetry: From the cyclic voltammograms, the specific capacitance was calculated by following equation: $C = (\int I\, dV)/\nu m\, \Delta V$, where C is the specific capacitance (F/g), I is the response current, ΔV is the potential window, ν is the CV scan rate (mV s^{-1}), and m is the mass of the electrode material(0.175 μg cm^{-2} per layer; mass of 65 layers with area 0.5 cm^{-2} = 0.5 cm^2 x 0.175 μg cm^{-2} x 65 layers = 5.68 μg).

Galvanostaitic charge-discharge measurement: From the galvanostatic charge/discharge curves, the specific capacitance of ruthenium complex multilayers was calculated by following equation:

$$C = \frac{I \times \Delta t}{\Delta V \times m}$$

where I is the current; Δt is the discharge time; ΔV is the potential window; m is the mass of the active material.

Based on the capacitance calculated, the energy density and power density were calculated using equation:

$$E = \frac{C(\Delta V)^2}{2}$$

where C is the specific capacitance of the active material, and ΔV is the voltage range of one sweep segment.

The power density was calculated using:

$$P = \frac{E}{\Delta t}$$

where E is the energy density and Δt is the corresponding discharge time in hours.

References:

(1) Shinomiya, T.; Ozawa, H.; Mutoh, Y.; Haga, M.-a. *Dalton Transactions* **2013**, *42*, 16166.

(2) Buttry, D. A.; Ward, M. D. *Chemical Reviews* **1992**, *92*, 1355.

(3) Lobo, R. F. M.; Pereira-da-Silva, M. A.; Raposo, M.; Faria, R. M.; Oliveira, O. N. *Nanotechnology* **1999**, *10*, 389.

(4) Hatzor, A.; Moav, T.; Cohen, H.; Matlis, S.; Libman, J.; Vaskevich, A.; Shanzer, A.; Rubinstein, I. *Journal of the American Chemical Society* **1998**, *120*, 13469.

(5) Nagashima, T.; Nakabayashi, T.; Suzuki, T.; Kanaizuka, K.; Ozawa, H.; Zhong, Y.-W.; Masaoka, S.; Sakai, K.; Haga, M.-a. *Organometallics* **2014**, *33*, 4893.

(6) (a) D. Lin-Vien, N.B. Colthup, W.G. Fateley, J.G. Grasselli "The handbook of infrared and Raman characteristic frequencies of organic molecules" Academic Press, London (**1991**). (b) S. Farquharson, K.L. Guyer, P.A. Lay, R.H. Nagnuson, M.J. Weaver *J. Am. Chem. Soc.* 1984, 106, 5123-5131. (c) R.R. Ruminski, C. Letner Inorg. Chim. Acta **1989**, 162, 175-177, (d) W.A. Alves, V. Pfaffen, P.I. Ortiz, S.I. Cordoba de Torresi, R.M. Torresi, *J. Braz. Chem. Soc*. **2008**, 19, 651-659, (e) M.S. Kim, M.K. Kim, C.J. Lee, Y.M. Jung, M.S. Lee, *Bull, Korean, Chem. Soc*. **2009**, 30, 2930-2934, (f) N.M. Aghatabay, A. Neshat, T. Karabiyik, M. Somer, D. Haciu, B. Dülger, *Euro. J. Med. Chem*. **2007**, 42, 205-213, (g) R.J. Davidson, E.W. Ainscough, A.M. Brodie, G.B. Jameson, M.R. Waterland, B. Moubaraki, K.S. Murray, K.C. Gordon, R. Horvath, G.N.L. Jameson, *Polyhedron* **2013**, 55, 37-44

(7) (a) I. Noda, J. Am. Chem. Soc. **1989**, 111, 8116-8118, (b) I. Noda, Kobunshi, **1990**, 39, 214-217, (c) I. Noda, Y. Liu, Y. Ozaki, *J. Phys. Chem*. 1996, 100, 8674-8680.

(8) 2D shige (C) Shigeaki Morita, Kwansei-Gakuin University, 2004-2005.